

High-performance broadband Faraday rotation spectroscopy of 2D materials and thin magnetic films

Benjamin Carey, Nils Kolja Wessling, Paul Steeger, Christoph Klusmann, Robert Schneider, Mario Fix, Robert Schmidt, Manfred Albrecht, Steffen Michaelis de Vasconcellos, Rudolf Bratschitsch, Ashish Arora

Angaben zur Veröffentlichung / Publication details:

Carey, Benjamin, Nils Kolja Wessling, Paul Steeger, Christoph Klusmann, Robert Schneider, Mario Fix, Robert Schmidt, et al. 2022. "High-performance broadband Faraday rotation spectroscopy of 2D materials and thin magnetic films." *Small Methods* 6 (11): 2200885. <https://doi.org/10.1002/smt.202200885>.

High-Performance Broadband Faraday Rotation Spectroscopy of 2D Materials and Thin Magnetic Films

Benjamin Carey, Nils Kolja Wessling, Paul Steeger, Christoph Klusmann, Robert Schneider, Mario Fix, Robert Schmidt, Manfred Albrecht, Steffen Michaelis de Vasconcellos, Rudolf Bratschitsch,* and Ashish Arora*

A Faraday rotation spectroscopy (FRS) technique is presented for measurements on the micrometer scale. Spectral acquisition speeds of about two orders of magnitude faster than state-of-the-art modulation spectroscopy setups are demonstrated. The experimental method is based on charge-coupled-device detection, avoiding speed-limiting components, such as polarization modulators with lock-in amplifiers. At the same time, FRS spectra are obtained with a sensitivity of 20 μrad (0.001 $^\circ$) over a broad spectral range (525–800 nm), which is on par with state-of-the-art polarization-modulation techniques. The new measurement and analysis technique also automatically cancels unwanted Faraday rotation backgrounds. Using the setup, Faraday rotation spectroscopy of excitons is performed in a hexagonal boron nitride-encapsulated atomically thin semiconductor WS_2 under magnetic fields of up to 1.4 T at room temperature and liquid helium temperature. An exciton g -factor of -4.4 ± 0.3 is determined at room temperature, and -4.2 ± 0.2 at liquid helium temperature. In addition, FRS and hysteresis loop measurements are performed on a 20 nm thick film of an amorphous magnetic $\text{Tb}_{20}\text{Fe}_{80}$ alloy.

instance spin, orbital, and valley magnetic moments) band structure of a material.^[2–7] Therefore, FR spectroscopy (FRS) is a powerful method in physics, chemistry, and biology. Some notable examples include the magnetic response and domain structures of solids,^[2,8] optically detected nuclear magnetic resonances in fluids,^[9,10] sensitive detection of paramagnetic molecules in gas mixtures,^[11] biochemical and for biomolecular detection,^[12] spin coherence probing in cold atoms,^[13,14] investigation of quantum spin fluctuations,^[15] and laser-frequency stabilization.^[16] It is also used to perform Zeeman spectroscopy of many-body quasiparticles in solids, such as neutral and charged excitons.^[2,17] As such, it is of fundamental importance to investigate the magnetic response of materials as a function of the photon energy.^[18] It is because their characteristic band structures have energy-dependent spin-polarized density of states and van Hove singularities which possess prominent magnetic responses.^[18,19] FRS provides this information with high sensitivity, under magnetic field (B) strengths of the order of 1 T or less, which are also suitable for device applications.^[2] With the recent advancements in the area of 2D semiconductors and magnets,^[17,20–26] FRS naturally emerges as a method for studying their magnetic-field-dependent band structures.

A major challenge while performing temperature-dependent (typically liquid He temperature up to room temperature)

1. Motivation

When linearly polarized light passes through a material held in a magnetic field applied in the direction of propagation of light, the plane of polarization of the light undergoes Faraday rotation (FR).^[1] It is because the material under a magnetic field offers different complex refractive indices to the circular components (σ^\pm) of the incident linear polarization.^[2] The transmitted light carries rich information on the magnetic-moment-resolved (for

B. Carey, N. K. Wessling, P. Steeger, C. Klusmann, R. Schneider, R. Schmidt, S. Michaelis de Vasconcellos, R. Bratschitsch, A. Arora
Institute of Physics and Center for Nanotechnology
University of Münster
48149 Münster, Germany
E-mail: rudolf.bratschitsch@uni-muenster.de

B. Carey
School of Mathematics and Physics
The University of Queensland
Saint Lucia, QLD 4072, Australia

 The ORCID identification number(s) for the author(s) of this article can be found under <https://doi.org/10.1002/smt.202200885>.

© 2022 The Authors. Small Methods published by Wiley-VCH GmbH. This is an open access article under the terms of the Creative Commons Attribution License, which permits use, distribution and reproduction in any medium, provided the original work is properly cited.

N. K. Wessling
Institute of Photonics
Department of Physics
University of Strathclyde
Glasgow G1 1RD, UK

M. Fix, M. Albrecht
Institute of Physics
University of Augsburg
86159 Augsburg, Germany

A. Arora
Department of Physics
Indian Institute of Science Education and Research
Pune 411008, India
E-mail: ashish.arora@iiserpune.ac.in

DOI: 10.1002/smt.202200885

micro-optical spectroscopy on 2D materials is that one has to keep the hexagonal boron nitride (hBN)-encapsulated 2D semiconductors^[27–29] spatially stable with sub-micrometer precision for the duration of the spectral acquisition.^[30] Normally, FRS is performed using modulation-based spectroscopy methods. Such measurements involve a polarization modulator, such as a photoelastic modulator, which periodically varies the state of polarization of the light incident on the sample.^[31] The transmitted or reflected monochromatic light is collected using a single-channel detector, such as a photomultiplier tube or a photodiode together with a lock-in amplifier (locked at the fundamental frequency f of the modulator or at $2f$). This technique provides a typical electronic-noise-limited sensitivity of about $35 \mu\text{rad}$ (0.002°) for measuring the rotation of the state of polarization.^[31,32] Since this technique requires scanning the wavelength of the light on the detector, recording an entire spectrum can take several hours. Hence, the spatial stability of the sample position on micrometer scales in the optical cryogen-flow or closed-cycle cryostats poses a severe challenge in this case over such long measurement times.

In this work, we overcome these challenges and perform high spatial and spectral-precision FRS on 2D semiconductors as well as thin magnetic-alloy films. Given the potential device-based applications of 2D semiconductors, it is imperative to perform Zeeman spectroscopy under device-relevant magnetic field strengths below 1 T. However, so far, existing investigations involve large magnetic fields (>5 T), because unmodulated methods such as magneto-photoluminescence (PL) or magneto-reflectance are used.^[17] Furthermore, since the exciton linewidths in 2D semiconductors such as monolayer WS_2 , WSe_2 , MoS_2 , MoSe_2 , and MoTe_2 are relatively large at room temperature (typically > 20 meV) compared to the Zeeman splittings (typically on the order of 2 meV at $B = 10$ T), almost all measurements are performed at liquid helium temperatures.^[17] At the same time, it is well known from GaAs that the Zeeman splittings of conduction and valence bands can depend strongly on the sample temperature.^[33,34] It still needs to be tested if this holds for 2D semiconductors such as monolayer WS_2 as well. Here, we perform FR-based Zeeman spectroscopy on an hBN-encapsulated WS_2 monolayer at room temperature and at cryogenic temperature ($T = 10$ K) up to an out-of-plane magnetic field of $B = 1.4$ T and determine the exciton g -factor. As another example, we perform FRS and spectrally resolved hysteresis-loop measurements on 20 nm thick films of an amorphous $\text{Tb}_{0.2}\text{Fe}_{0.8}$ alloy to demonstrate the capabilities of our method to investigate magnetic materials as well.

2. Experimental Setup

Our new measurement technique involves a charge-coupled device (CCD)-based signal acquisition, in contrast to conventional polarization-modulation spectroscopy, which employs lock-in amplifiers. Simultaneous wavelength-dispersed data recording of the circular polarizations σ^+ and σ^- by the same CCD chip provides many orders of magnitude higher spectral accumulation speeds (1–2 min per spectrum) when compared with lock-in-based methods (several hours per spectrum). Additionally, the simultaneous recording of both polarization directions cancels out noise, which is induced by, e.g., intensity fluctuations of the

light source (similar to an autobalanced detection), yielding shot-noise-limited sensitivity. The specific arrangement of the optical elements and our measurement scheme also solve the problem of removing unwanted Faraday rotation backgrounds from the signal. A detailed description of our setup is as follows.

A schematic drawing of the setup is displayed in **Figure 1**. Broadband light from a 75 W xenon arc lamp is collimated and linearly polarized at $P = 45^\circ$ after passing through a sheet polarizer P. It then enters a 30 mm diameter hole H1 from the side of an electromagnet (maximum field = 1.4 T, pole gap = 47 mm). The light passes through an 80 mm focal length achromatic-doublet lens L2 (400–700 nm antireflection coated) installed within the magnet's hole. It is focused on the sample, which is mounted on the extended cold finger of a continuous-flow cryostat, after exiting through a 10 mm diameter hole H2 in the pole piece of the magnet. The sample plane (x - y plane) is normal to the direction of the magnetic field (z -direction) for performing measurements in Faraday geometry. A 7 mm diameter hole in the copper cold finger (not shown) lets the light transmit through the sample S. The cold

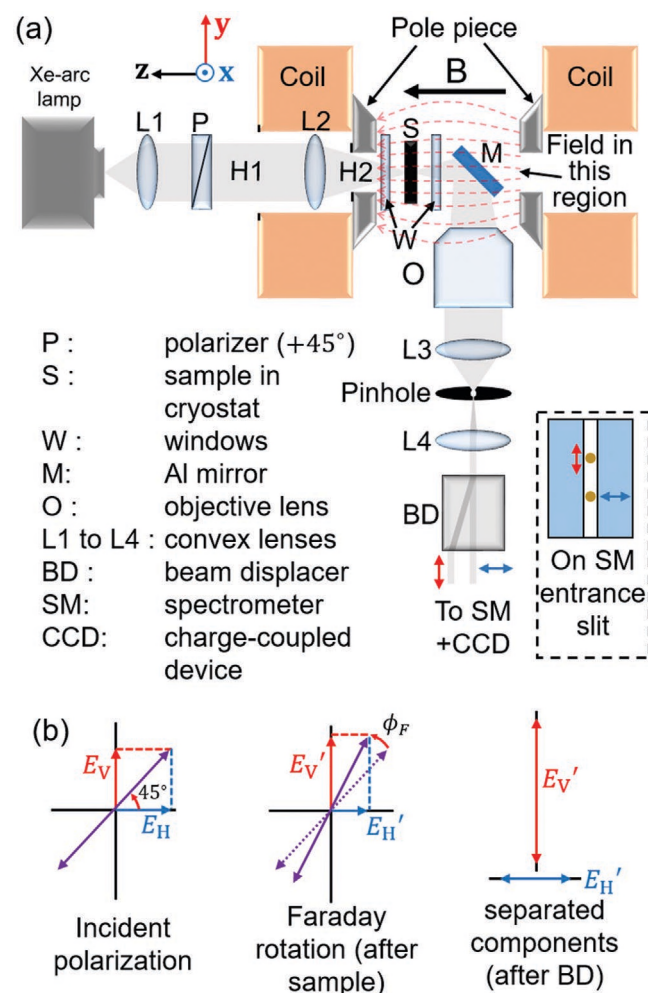


Figure 1. Schematic of the Faraday rotation spectroscopy setup. a) Schematic (top view) of the Faraday rotation spectroscopy setup depicting the arrangement of the key components. The inset (dashed lines) shows the focused spots corresponding to the two polarization components split by the beam displacer (BD) at the entrance slit of the spectrometer (SM). b) Polarization state of the light after passing through the sample and the beam displacer.

finger is enclosed in a polished nonmagnetic stainless steel cold shield and a vacuum shield with two 1 mm thick *c*-plane (0001) sapphire windows around the sample. After passing through the sample under vacuum, the light undergoes a reflection from an aluminum mirror M and is steered by 90°. It is then collimated by a long working distance (34 mm) 10× objective lens O (numerical aperture, NA = 0.28, focal length = 20 mm). A *z*-translation stage attached to the cryostat is used to move the sample to the focal plane of the objective lens. The collimated light is focused on a 20 μm diameter pinhole using a 100 mm focal length achromatic-doublet lens L3 (400–1100 nm antireflection coated). The light transmitting through the pinhole is collimated again with another lens L4 (same technical specifications as L3). This arrangement selects light from a spot of 4 μm diameter on the sample. This spatial resolution can be improved further by selecting a smaller pinhole or a larger focal length of L3. The light then passes through a beam displacer (BD), acting as an analyzer which spatially splits the beam by 0.6 mm into two orthogonal linearly polarized beams (see Figure 1b). A 150 mm focal length achromatic-doublet lens (not shown) finally focuses the light on a 50 μm wide slit of a 0.3 m focal length spectrometer (Figure 1a, inset). The spectra corresponding to the two polarization directions are imaged onto different rows of a Peltier-cooled (*T* = 200 K) CCD mounted at the exit port of the spectrometer and are recorded simultaneously. As described in the following section, we measure the signals in two configurations of applied magnetic fields in order to simplify the spectral analysis.

2.1. Statistical Analysis

The statistical and data analysis details are provided in sections 4 and 5 at appropriate locations. Wolfram Mathematica 9 is used for writing programs for data analysis.

3. Method

To explain the functionality of the new Faraday rotation spectroscopy setup, a Jones matrix analysis is performed as follows.^[35] The Jones' matrices of various components in the setup with magnetic field applied along the +*z*-direction (*B*⁺) in Figure 1 following ref. [32] are

$$\text{Incident polarized light : } \hat{P}(p) = E_0 \begin{bmatrix} \cos p \\ \sin p \end{bmatrix} \quad (1)$$

where *E*₀ is the incident electric field

$$\text{Sample : } \hat{S}(B^+) = \begin{bmatrix} 1 & -\Phi_F \\ \Phi_F & 1 \end{bmatrix} \quad (2)$$

$$\text{Mirror : } \hat{M} = \begin{bmatrix} \tan \Psi e^{i\Delta} & 0 \\ 0 & -1 \end{bmatrix} \quad (3)$$

$$\text{Beam displacer : } \widehat{BD}(a) = \begin{bmatrix} \cos^2 a & \cos a \sin a \\ \cos a \sin a & \sin^2 a \end{bmatrix}, \quad (4)$$

where *a* = 0° or 90°

Here $\Phi_F = \phi_F + i\eta_F$ is the complex Faraday rotation of the sample, while ϕ_F and η_F are the Faraday rotation and the Faraday ellipticity.^[2] $\tan \Psi$ and Δ are the ellipsometry parameters of the aluminum mirror.^[32] The electric field amplitudes (*E*_H' and *E*_V') for the two BD-split polarizations reaching the CCD chip are proportional to

$$E'_H \propto \widehat{BD}(0^\circ) \cdot \hat{M} \cdot \hat{S} \cdot \hat{P}(45^\circ) \quad (5)$$

$$E'_V \propto \widehat{BD}(90^\circ) \cdot \hat{M} \cdot \hat{S} \cdot \hat{P}(45^\circ) \quad (6)$$

The detected intensities for the two detected polarizations are proportional to $I_H = E'_H \cdot E'_H$ and $I_V = E'_V \cdot E'_V$. We define

$$\Delta I = I_H - I_V \text{ and } I = \frac{I_H + I_V}{2} \quad (7)$$

Let us consider that I_H^0 and I_V^0 are the intensities of the transmitted light for the two polarizations without the sample. Using

$$\Delta I^0 = I_H^0 - I_V^0 \text{ and } I^0 = \frac{I_H^0 + I_V^0}{2} \quad (8)$$

we can calculate the following quantity

$$\delta(B^+) = \frac{\Delta I}{I} - \frac{\Delta I^0}{I^0} \sim \frac{16 \tan^2 \Psi \phi_F}{(1 + \tan^2 \Psi)(1 + \tan^2 \Psi + 2\phi_F(1 - \tan^2 \Psi))} + \phi_{bg} \quad (9)$$

where we assume a negligibly small value of ϕ_F and η_F compared to 1, so that second-order terms in ϕ_F and η_F are neglected. Here, ϕ_{bg} is a background signal which originates from the imperfections in the setup such as i) small strain in the optics and windows leading to linear birefringence, and ii) a slight misalignment in the angles of the polarizer/BD analyzer. This background signal can sometimes be quite high compared to the actual Faraday rotation ϕ_F .^[8] Since this background signal is independent of the direction of the magnetic field, it can be removed by making two measurements for the opposite directions of the applied magnetic fields, i.e., *B*⁺ and *B*[−] along +*z* and −*z*, respectively. The Jones' matrix of the sample for *B*[−] is

$$\hat{S}(B^-) = \begin{bmatrix} 1 & \Phi_F \\ -\Phi_F & 1 \end{bmatrix} \quad (10)$$

For this case, the Jones' matrix analysis yields

$$\delta(B^-) \sim \frac{16 \tan^2 \Psi \phi_F}{(1 + \tan^2 \Psi)(1 + \tan^2 \Psi - 2\phi_F(1 - \tan^2 \Psi))} + \phi_{bg} \quad (11)$$

We can calculate the Faraday rotation ϕ_F from the following quantity

$$\delta = \frac{\delta(B^+) - \delta(B^-)}{2} \sim \frac{16 \tan^2 \Psi}{(1 + \tan^2 \Psi)^2} \phi_F \quad (12)$$

Hence, the Faraday rotation ϕ_F can be determined, provided that the $\tan \Psi$ parameter of the mirror is known. For the case

of an aluminum mirror, which we use for our measurements in this work, $\tan \Psi$ is between 0.95 and 0.97 in the wavelength range of 500–800 nm.^[36] In this case, Equation (12) approximately yields

$$\delta(\text{Al Mirr}) \approx 3.987 - 3.993 \phi_F \quad (13)$$

which is nearly $3.99 \phi_F$ within 0.1% over the wavelength range of 500 – 800 nm.

To summarize the above discussion for obtaining a Faraday rotation spectrum, we have to perform four measurements using the setup in Figure 1: i) measure I_H and I_V when light passes through the sample (Equation (7)) with B^+ applied magnetic field, ii) measure I_H and I_V when light passes through the sample (Equation (7)) with B^- applied field, iii) measure I_H^0 and I_V^0 when light passes through air or bare substrate (Equation (8)) with B^- applied field, iv) measure I_H^0 and I_V^0 when light passes through air or bare substrate (Equation (8)) with B^+ applied field. In each of these steps, light is collected by the CCD for an integration time t_{int} , yielding the total measurement time equal to $t = 4t_{\text{int}}$. Thereafter, Faraday rotation is calculated using Equation (12). An example of the step-by-step procedure to deduce the Faraday rotation is shown in Figure S1 (Supporting Information). The Faraday rotation background due to the rotation of light from the optical components inside the magnetic field is eliminated in our method. Otherwise, one can have very large FR backgrounds (many degrees) due to thick optics and the substrate directly within the magnetic field.^[8]

4. Quantitative Verification of the Method

To demonstrate the quantitative functionality of our new method based on Equation (12), we perform the following experiment. In our setup in Figure 1a, we replace the sample with an achromatic half-wave plate (HWPR) and use it as a calibrated polarization rotator (instead of the sample under magnetic fields). This allows us to precisely set specific rotation values across the entire broad wavelength range, which is key for calibrating the setup. When the HWPR's fast axis is aligned along the direction of incident polarization (at 45° with respect to the x -direction), there is no net rotation. However, a rotation of the HWPR by an angle θ with respect to the incidence polarization results in a rotation by 2θ . The HWPR is rotated manually in steps of $\theta = 0.5^\circ$. After each step, the rotation of the incident polarized beam is measured using two methods: the null method (Figure 2a) and the presented method (Figure 1). The measurement using the null method is done in steps of 25 nm from 525 to 825 nm, which is the working range of this broadband HWPR. These results (solid spheres in Figure 2b) are compared with the results using the presented method (solid lines in Figure 2b). An excellent agreement between the two methods until $\theta = 3^\circ$ confirms the accuracy of our method. A deviation of rotation from the ideal 2θ value in wavelengths from 525 to 575 nm in Figure 2b is due to limitations of the HWPR in setting a half-wave retardation accurately in this wavelength region.

a) Optical scheme for the null method

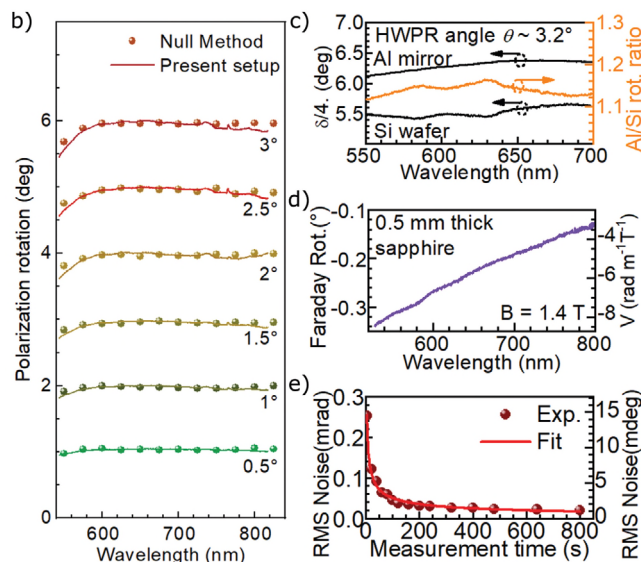
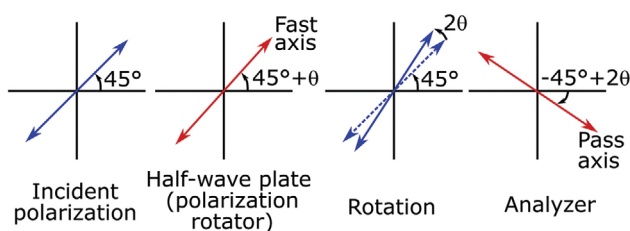


Figure 2. Quantitative test of the method. a) Optical scheme of the null method used to verify the quantitative working of our setup in Figure 1. A broadband achromatic half-wave plate (HWPR) is used as a rotator, in place of the sample. b) Comparison of the optical rotation 2θ introduced by the half-wave plate rotation by θ using the null method in panel (a) and the present method. The excellent agreement verifies the applicability of our method. c) Left axis: $\delta/4$ measured by a setting the HWPR angle $\theta \approx 3.2^\circ$ using an Al mirror and replacing it with a polished Si wafer. For the Al mirror, $\delta/4$ is nearly equal to the actual value of rotation as explained in the text. Right axis: Ratio of rotations measured in the two cases. The factor between 1.12 and 1.16 in the wavelength range of the measurement is in agreement with the theory. The different wavelength ranges in panels (b) and (c) are due to different HWPRs used in the two cases. d) An example of a Faraday rotation spectrum of a 0.5 mm thick c -cut double-polished sapphire crystal under a magnetic field of 1.4 T with an integration time of 30 s and hence a total measurement time t of 120 s. Similar spectra are measured for other measurement times. The right axis denotes the Verdet constant (V) in units of $\text{rad m}^{-1} \text{T}^{-1}$. e) Spectra such as in panel (d) are used to determine root-mean-square noise (spheres) in the Faraday rotation spectra as a function of measurement time. The solid line is the $1/\sqrt{t}$ fit to the data, suggesting that our measurement is limited by shot noise.

4.1. Influence of Ellipsometry Parameters of the Mirror

To reveal the effect of the ellipsometry parameter $\tan \Psi$ in Equation (2), we perform the following measurement. We rotate the HWPR to a certain value (close to 3.2° in this case), which introduces a rotation of $6.2^\circ - 6.4^\circ$ in the wavelength range from 550 to 700 nm (the working range of this HWPR). The rotation is measured using the method described in Figure 1, where two types of mirrors M are used: front-polished aluminum and a polished Si wafer. We plot $\delta/4$ from the

two measurements as solid black lines in Figure 2c and notice that the curve measured when using the Si wafer is lower than that of the Al mirror by a factor lying between 1.12 and 1.16 (orange line in Figure 2c). This is explained as follows. We note from Equation (13) that the expected $\delta/4$ using the Al mirror is approximately ϕ_F . In the case of the Si wafer, the $\tan \Psi$ parameter lies between 0.69 and 0.7 in the wavelength range of 550–700 nm.^[36] This yields

$$\delta(\text{Si Mirr}) \approx 3.49 - 3.53 \phi_F \quad (14)$$

within the wavelength range. Therefore, $\delta(\text{Al Mirr})/\delta(\text{Si Mirr})$ is expected to be ≈ 1.13 – 1.15 , which is in excellent agreement with our experimental value. This further justifies the applicability of Equation (12) to our analysis.

We would like to stress that our measurement protocol also solves a common problem of modulation FRS or MOKE spectroscopy.^[32] In these methods, the presence of mirror M leads to a mixing of the rotation and ellipticity signals via the ellipsometry parameters $\tan \Psi$ and Δ of the mirror.^[32] This requires a nontrivial signal analysis to deduce the actual rotation and ellipticity. In our method, there is no dependence on the Δ parameter of the mirror, which makes the signal analysis easy compared to the traditional methods.^[32]

4.2. Root-Mean-Square Noise

To estimate the root-mean-square (RMS) noise in our measurements, we measure the Faraday rotation of 0.5 mm thick *c*-cut sapphire in the 525–800 nm wavelength range under a magnetic field of $B = 1.4$ T as a function of integration time. An example of a spectrum obtained in this manner is shown in Figure 2d for the total measurement time $t = 4 t_{\text{int}} = 120$ s, where t and t_{int} have been defined in the “Method” section. RMS noise is calculated in the Faraday rotation spectra as a function of measurement time (spheres in Figure 2e). The noise follows a $1/\sqrt{t}$ function, elucidating that the measurements are shot-noise limited. The RMS noise in the spectra is found to be better than 0.002° (or $35 \mu\text{rad}$) for measurement times ≥ 250 s. For this short measurement time, this is already comparable to the state-of-the-art modulation spectroscopy techniques.^[31,32] For longer accumulation times, the performance gets much better, while still requiring orders of magnitude shorter measurement times compared to the modulation methods. For instance, we acquire FR spectra with 1024 wavelength steps (total CCD pixels in a row) using our method in about 4 min. However, such a spectrum with a similar signal-to-noise ratio obtained using modulation spectroscopy would require about 8–9 h (previous experience of the authors^[32,37,38]), which is more than two orders of magnitude longer accumulation time.

5. Faraday Rotation Spectroscopy of an hBN-Encapsulated WS_2 Monolayer

To demonstrate the capabilities of the new Faraday rotation setup, we measure the valley Zeeman splitting and valley polarization effects on excitons in an atomically thin transi-

tion metal dichalcogenide semiconductor. We prepare an hBN-encapsulated WS_2 monolayer on a 0.5 mm thick *c*-cut sapphire substrate.^[39] The room-temperature ($T = 295$ K) and low-temperature ($T = 10$ K) optical transmission spectra of the sample are shown in Figure 3a and Figure 3e, respectively. The strong response due to the ground-state neutral A exciton X_A^0 is identified as a sharp drop in optical transmittance. The full-width at half-maximum (FWHM) linewidths of the exciton resonance are 22 and 6.1 meV for 295 and 10 K, respectively. The corresponding FR spectra are depicted in Figure 3b,f for magnetic fields from $B = 0.2 - 1.4$ T ($0.2 - 1.2$ T for the low-temperature measurement). We emphasize that such FR spectra would be almost impossible to be measured on these samples using traditional modulation spectroscopy as in refs. [37,38], since many hours of sample stability on sub-micrometer levels are impractical in free-space magneto-optics setups.

The FR spectra are fitted using a transfer-matrix-based analysis technique, similar to the one described in ref. [37] for MOKE spectroscopy of excitons in GaAs quantum wells. The complex Fresnel transmission coefficients \tilde{t}_{σ^\pm} of the sample for the circular σ^+ and σ^- polarizations can be written as

$$\tilde{t}_{\sigma^\pm} = t_{\sigma^\pm} e^{i\theta_{\sigma^\pm}} \quad (15)$$

The Faraday rotation of the light when passing through the sample is related to the phases θ_{σ^\pm} as

$$\phi_F = -\frac{1}{2}(\theta_{\sigma^+} - \theta_{\sigma^-}) \quad (16)$$

To derive θ_{σ^\pm} , first, the transmittance spectrum is simulated. Assuming that the excitonic contribution to the dielectric function of the material is given by a complex Lorentz oscillator, the dielectric response function of the sample is^[37]

$$\varepsilon(E) = (n_b + ik_b)^2 + \frac{A}{E_0^2 - E^2 - i\gamma E} \quad (17)$$

where E_0 , A , and γ are the exciton transition energy, integrated absorption intensity, and linewidth parameters, respectively. $n_b + ik_b$ is the background complex refractive index of a WS_2 monolayer without excitons.^[40,41] The fitted transmittance spectra around the A exciton using the transfer-matrix technique are shown as black solid lines in Figure 3a,e. The Fresnel coefficient \tilde{t} is obtained from the fit, and the phase θ is derived (Equation (15)). An application of a magnetic field leads to a valley Zeeman splitting

$$\Delta E = E_{\sigma^+} - E_{\sigma^-} = g_x \mu_B B \quad (18)$$

and a valley polarization^[17]

$$(A_{\sigma^+} - A_{\sigma^-}) / (A_{\sigma^+} + A_{\sigma^-}) = \Delta A / 2A \quad (19)$$

Here, E_{σ^\pm} and A_{σ^\pm} are the exciton transition energies and the oscillator strength parameters, g_x is the effective g factor of the exciton, and $\mu_B = 0.05788$ meV T^{-1} is the Bohr's magneton. These effects result in a difference in the phases θ_{σ^\pm} and a characteristic Faraday rotation ϕ_F spectral line shape (Equation (16)).

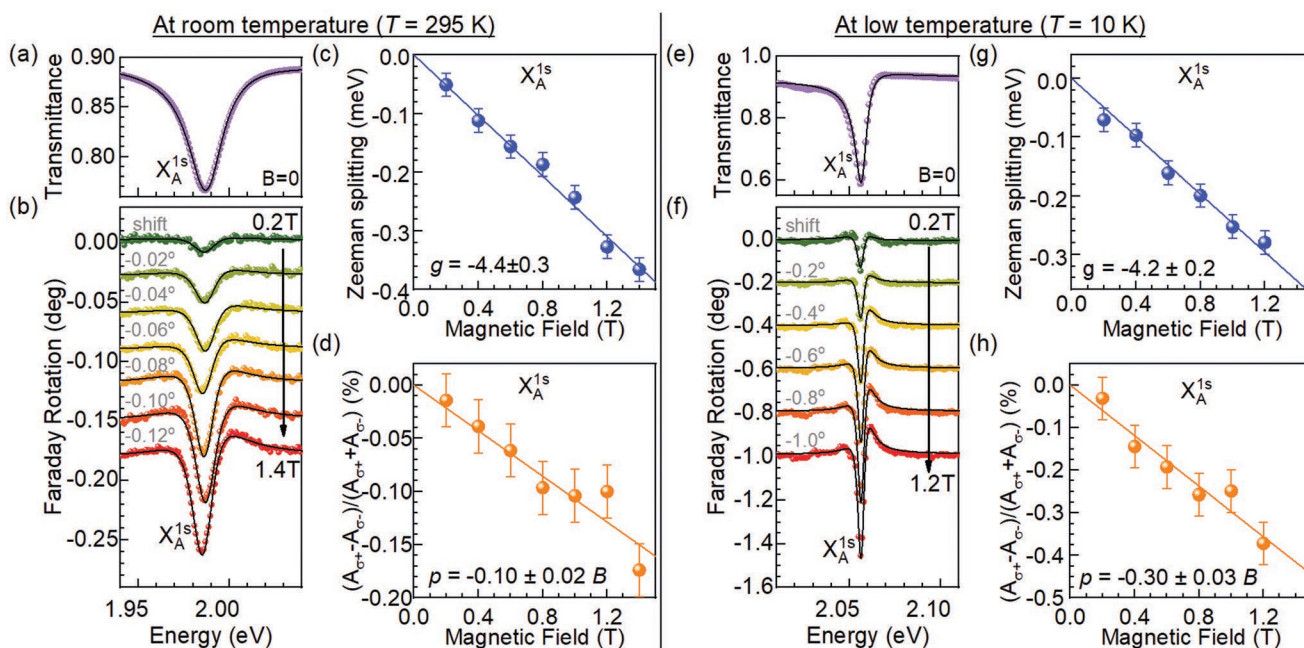


Figure 3. Faraday rotation spectroscopy of an hBN-encapsulated WS₂ monolayer. a) Experimental (purple spheres) and modeled (black solid line) optical transmittance spectra of an hBN-encapsulated WS₂ monolayer for $B = 0$ T at $T = 295$ K. The neutral exciton X_A^{1s} absorbs strongly around 1.988 eV. b) Experimental (solid spheres) and simulated (solid lines) Faraday rotation spectra of the hBN-encapsulated WS₂ monolayer from $B = 0$ to 1.4 T. The curves are vertically shifted for clarity by the indicated value. c) Valley Zeeman splitting and d) magnetic-field-induced valley polarization of X_A^{1s} applying the line shape modeling in panel (b). Solid lines in panels (c) and (d) are the fits to the data illustrating the linear change in valley Zeeman splitting and polarization within the field range studied. e–h) Similar to panels (a)–(d), respectively, but at a low temperature of $T = 10$ K. Faint wiggles around 2.03 eV in panels (e) and (f) originate due to charged excitons.^[17] However, they are not analyzed in this work due to their weak signature. The g -factors of X_A^{1s} obtained at $T = 295$ K and $T = 10$ K are -4.4 ± 0.3 and -4.2 ± 0.2 , respectively.

For instance, a nonzero ΔE causes a dip in the Faraday rotation spectra at various magnetic fields in Figure 3b,f. The depth of this dip increases with rising magnetic field, since the excitonic Zeeman splitting increases. On the other hand, a non-zero $\Delta A/2A$ results in a shoulder to this dip on the high-energy side. The spectral line shapes are fitted in Figure 3b,f (solid lines) to determine the magnetic-field-induced exciton Zeeman splitting and polarization. The Zeeman splittings are plotted in Figure 3c,g, while the valley polarizations are plotted in Figure 3d,h. The exciton g -factor is found to be -4.4 ± 0.3 and -4.2 ± 0.2 at $T = 295$ and 10 K, respectively, after fitting the B -dependent Zeeman splitting in Figure 3c,g with a linear function. The largest source of error in determining these numbers is the fitting error in the line shape modeling of the FR spectra.^[37,38] The value of the exciton g -factor is in excellent agreement with previous measurements at liquid He temperatures.^[17,42–44] We notice that we do not obtain different g -factors at the two temperatures studied. This is unlike the previously studied bulk GaAs,^[33,34] and will become a matter of future studies. The exciton valley polarization increases linearly with a slope of $p = -0.1 \pm 0.02\%$ and $-0.3 \pm 0.03\%$ T⁻¹ at $T = 295$ K (Figure 3d) and 10 K (Figure 3h), respectively. These results highlight the sensitivity of our method, since we are able to measure extremely small Zeeman splittings such as 50 μ eV at $B = 0.2$ T in Figure 3c, with ± 20 μ eV accuracy and tiny valley polarizations such as 0.05% at $B = 0.4$ T in Figure 3d with $\pm 0.02\%$ accuracy. In comparison, other methods reported in the literature such as magnetorefectance yield limited accuracies of about ± 100 μ eV and $\pm 1\%$, respectively.^[44–46]

6. Faraday Rotation Spectroscopy of a Tb₂₀Fe₈₀ Alloy Thin Film

To demonstrate the suitability of our setup in performing state-of-the-art FRS and hysteresis loop measurements on a magnetic film, we measure the Faraday rotation spectrum of a 20 nm thick film of an amorphous ferrimagnetic Tb₂₀Fe₈₀ alloy grown on a 500 μ m thick c -cut double-side polished sapphire substrate with a 5 nm platinum seed layer. The sample is prepared by magnetron sputtering at room temperature and exhibits an out-of-plane easy axis of magnetization. To avoid oxidation, the layer stack is capped by 5 nm Si₃N₄. Further details of the sample preparation can be found in ref. [47]. The sample transmits 7 – 75% of the light in the spectral range measured (500 – 775 nm) (Figure 4). At the highest magnetic field available (1.4 T), the magnetization of the film is completely saturated. The magnitude of the Faraday rotation rises almost linearly from 0.1° to 0.55° with increasing wavelength in the investigated spectral range (Figure 4a). Magnetization hysteresis measurements are performed by sweeping the magnetic field from +1.4 to -1.4 T, and back to +1.0 T. The measured hysteresis curves at several different wavelengths are shown in Figure 4b. A sudden reversal of the Faraday rotation at $B = 0.25$ T along out-of-plane direction is observed, leading to a steep hysteresis curve. The data are in excellent agreement with the hysteresis loop measurement, performed by the superconducting quantum interference device–vibrating sample magnetometry (SQUID–VSM) shown in Figure 4b.

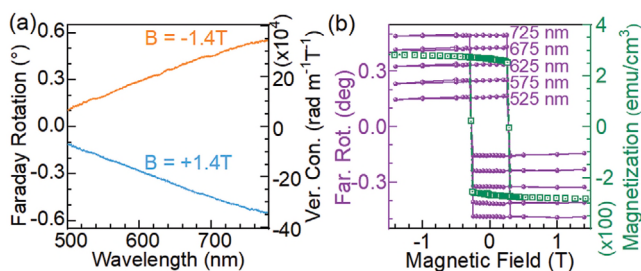


Figure 4. Faraday rotation spectroscopy and out-of-plane hysteresis loop of a ferrimagnetic $\text{Tb}_{20}\text{Fe}_{80}$ alloy thin film. a) Faraday rotation spectra of a 20 nm thick $\text{Tb}_{0.2}\text{Fe}_{0.8}$ alloy film on a 0.5 mm thick sapphire substrate at magnetic fields of +1.4 and -1.4 T. b) Left axis (purple): Hysteresis loops plotted for five different wavelengths to demonstrate the proof of concept. Right axis (green): Hysteresis loop obtained using SQUID-VSM magnetometry showing excellent agreement with the Faraday rotation data.

7. Conclusion

In conclusion, we have presented a novel experimental setup for performing Faraday rotation spectroscopy at microscopic spatial resolutions. It is capable of performing measurements with 2–3 orders of magnitude enhanced speeds compared to traditional photoelastic-modulator-based setups, while yielding a comparable signal-to-noise ratio. The setup is ideal to perform Zeeman spectroscopy of 2D semiconductors, as well as for hysteresis loop measurements of magnetic thin films. Our work provides a significant advancement in magneto-optics spectroscopy and opens pathways to optical investigations of spintronic and valleytronic phenomena on micrometer length scales with high speed and precision.

Supporting Information

Supporting Information is available from the Wiley Online Library or from the author.

Acknowledgements

The authors acknowledge the financial support from the German Research Foundation (DFG Project Nos. AR 1128/1-1 and AR 1128/1-2), the Alexander von Humboldt foundation, and NM-ICPS of the DST, Government of India through the I-HUB Quantum Technology Foundation (Pune, India).

Open access funding enabled and organized by Projekt DEAL.

Conflict of Interest

The authors declare no conflict of interest.

Data Availability Statement

The data that support the findings of this study are available from the corresponding author upon reasonable request.

Keywords

beam displacer, CCD, excitons, Faraday rotation, transition metal dichalcogenides, WS_2

Received: July 7, 2022
Revised: September 21, 2022
Published online: October 13, 2022

- [1] M. I. Faraday, *Philos. Trans. R. Soc. London* **1846**, 136, 1.
- [2] H. Piller, in *Semiconductors and Semimetals*, (Eds: R. K. Willardson, A. C. Beer), Vol. 8, Academic Press, New York, NY **1972**, pp. 103–179.
- [3] B. Lax, Y. Nishina, *Phys. Rev. Lett.* **1961**, 6, 464.
- [4] I. M. Boswarva, R. E. Howard, A. B. Lidiard, *Proc. R. Soc. London, Ser. A* **1962**, 269, 125.
- [5] L. M. Roth, *Phys. Rev.* **1964**, 133, A542.
- [6] H. S. Bennett, E. A. Stern, *Phys. Rev.* **1965**, 137, A448.
- [7] P. S. Pershan, *J. Appl. Phys.* **1967**, 38, 1482.
- [8] J. Černe, D. C. Schmadel, L. B. Rigal, H. D. Drew, *Rev. Sci. Instrum.* **2003**, 74, 4755.
- [9] I. M. Savukov, S.-K. Lee, M. V. Romalis, *Nature* **2006**, 442, 1021.
- [10] D. Pagliero, W. Dong, D. Sakellariou, C. A. Meriles, *J. Chem. Phys.* **2010**, 133, 154505.
- [11] R. Lewicki, J. H. Doty, R. F. Curl, F. K. Tittel, G. Wysocki, *Proc. Natl. Acad. Sci. USA* **2009**, 106, 12587.
- [12] R. J. Murdock, S. A. Putnam, S. Das, A. Gupta, E. D. Z. Chase, S. H.-T. Seal, *Small* **2017**, 13, 1602862.
- [13] M. Swar, D. Roy, S. Bhar, S. Roy, S. Chaudhuri, *Phys. Rev. Res.* **2021**, 3, 043171.
- [14] G. Labeyrie, C. Miniatura, R. Kaiser, *Phys. Rev. A* **2001**, 64, 033402.
- [15] S.-W. Chen, R.-B. Liu, *Sci. Rep.* **2015**, 4, 4695.
- [16] W. Quan, Y. Li, R. Li, H. Shang, Z. Fang, J. Qin, S. Wan, *Appl. Opt.* **2016**, 55, 2503.
- [17] A. Arora, *J. Appl. Phys.* **2021**, 129, 120902.
- [18] A. Molina-Sánchez, G. Catarina, D. Sangalli, J. Fernández-Rossier, *J. Mater. Chem. C* **2020**, 8, 8856.
- [19] J. Singh, *Electronic and Optoelectronic Properties of Semiconductor Structures*, Cambridge University Press, New York, NY **2003**.
- [20] J. R. Schaibley, H. Yu, G. Clark, P. Rivera, J. S. Ross, K. L. Seyler, W. Yao, X. Xu, *Nat. Rev. Mater.* **2016**, 1, 16055.
- [21] C. C. Mayorga-Martinez, Z. Sofer, D. Sedmidubský, Š. Huber, A. Y. S. Eng, M. Pumera, *ACS Appl. Mater. Interfaces* **2017**, 9, 12563.
- [22] N. R. Pradhan, S. Talapatra, M. Terrones, P. M. Ajayan, L. Balicas, *IEEE Nanotechnol. Mag.* **2017**, 11, 18.
- [23] G. Wang, A. Chernikov, M. M. Glazov, T. F. Heinz, X. Marie, T. Amand, B. Urbaszek, *Rev. Mod. Phys.* **2018**, 90, 021001.
- [24] M. Gibertini, M. Koperski, A. F. Morpurgo, K. S. Novoselov, *Nat. Nanotechnol.* **2019**, 14, 408.
- [25] S. Liu, K. Yang, W. Liu, E. Zhang, Z. Li, X. Zhang, Z. Liao, W. Zhang, J. Sun, Y. Yang, H. Gao, C. Huang, L. Ai, P. K. J. Wong, A. T. S. Wee, A. T. N'Diaye, S. A. Morton, X. Kou, J. Zou, Y. Xu, H. Wu, F. Xiu, *Natl. Sci. Rev.* **2020**, 7, 745.
- [26] B. Huang, M. A. McGuire, A. F. May, D. Xiao, P. Jarillo-Herrero, X. Xu, *Nat. Mater.* **2020**, 19, 1276.
- [27] O. A. Ajayi, J. V. Ardelean, G. D. Shepard, J. Wang, A. Antony, T. Taniguchi, K. Watanabe, T. F. Heinz, S. Strauf, X.-Y. Zhu, J. C. Hone, *2D Mater.* **2017**, 4, 031011.
- [28] J. Wierzbowski, J. Klein, F. Sigger, C. Straubinger, M. Kremser, T. Taniguchi, K. Watanabe, U. Wurstbauer, A. W. Holleitner, M. Kaniber, K. Müller, J. J. Finley, *Sci. Rep.* **2017**, 7, 12383.
- [29] F. Cadiz, E. Courtade, C. Robert, G. Wang, Y. Shen, H. Cai, T. Taniguchi, K. Watanabe, H. Carrere, D. Lagarde, M. Manca,

- T. Amand, P. Renucci, S. Tongay, X. Marie, B. Urbaszek, *Phys. Rev. X* **2017**, *7*, 021026.
- [30] S. Shree, I. Paradisanos, X. Marie, C. Robert, B. Urbaszek, *Nat. Rev. Phys.* **2020**, *3*, 39.
- [31] K. Sato, *Jpn. J. Appl. Phys.* **1981**, *20*, 2403.
- [32] A. Arora, S. Ghosh, V. Sugunakar, *Rev. Sci. Instrum.* **2011**, *82*, 123903.
- [33] M. Oestreich, W. W. Ruhle, *Phys. Rev. Lett.* **1995**, *74*, 2315.
- [34] W. Zawadzki, P. Pfeffer, R. Bratschitsch, Z. Chen, S. T. Cundiff, B. N. Murdin, C. R. Pidgeon, *Phys. Rev. B* **2008**, *78*, 245203.
- [35] E. Hecht, *Optics*, 4th ed., Pearson Addison Wesley, Reading, MA **2001**.
- [36] A. Arora, S. Ghosh, *Rev. Sci. Instrum.* **2010**, *81*, 123102.
- [37] A. Arora, A. Mandal, S. Chakrabarti, S. Ghosh, *J. Appl. Phys.* **2013**, *113*, 213505.
- [38] A. Arora, N. Hatui, A. Bhattacharya, S. Ghosh, *Appl. Phys. Lett.* **2013**, *103*, 052109.
- [39] A. Arora, N. K. Wessling, T. Deilmann, T. Reichenauer, P. Steeger, P. Kossacki, M. Potemski, S. M. de Vasconcellos, M. Rohlfing, R. Bratschitsch, *Phys. Rev. B* **2020**, *101*, 241413.
- [40] Y. Li, A. Chernikov, X. Zhang, A. Rigosi, H. M. Hill, A. M. van der Zande, D. A. Chenet, E.-M. Shih, J. Hone, T. F. Heinz, *Phys. Rev. B* **2014**, *90*, 205422.
- [41] Y. Niu, S. Gonzalez-Abad, R. Frisenda, P. Maruhn, M. Drüppel, P. Gant, R. Schmidt, N. Taghavi, D. Barcons, A. Molina-Mendoza, S. de Vasconcellos, R. Bratschitsch, D. Perez De Lara, M. Rohlfing, *Nanomaterials* **2018**, *8*, 725.
- [42] R. Schmidt, A. Arora, G. Plechinger, P. Nagler, A. Granados Del Águila, M. V. Ballottin, P. C. M. Christianen, S. Michaelis De Vasconcellos, C. Schüller, T. Korn, R. Bratschitsch, *Phys. Rev. Lett.* **2016**, *117*, 077402.
- [43] G. Plechinger, P. Nagler, A. Arora, A. Granados del Águila, M. V. Ballottin, T. Frank, P. Steinleitner, M. Gmitra, J. Fabian, P. C. M. Christianen, R. Bratschitsch, C. Schüller, T. Korn, *Nano Lett.* **2016**, *16*, 7899.
- [44] M. Koperski, M. R. Molas, A. Arora, K. Nogajewski, M. Bartos, J. Wyzula, D. Vaclavkova, P. Kossacki, M. O. Potemski, *2D Mater.* **2018**, *6*, 015001.
- [45] A. Arora, M. Koperski, A. Slobodeniuk, K. Nogajewski, R. Schmidt, R. Schneider, M. R. Molas, S. M. de Vasconcellos, R. Bratschitsch, M. Potemski, *2D Mater.* **2019**, *6*, 015010.
- [46] G. Wang, L. Bouet, M. M. Glazov, T. Amand, E. L. Ivchenko, E. Palleau, X. Marie, B. Urbaszek, *2D Mater.* **2015**, *2*, 034002.
- [47] R. Schneider, M. Fix, R. Heming, S. M. de Vasconcellos, M. Albrecht, R. Bratschitsch, *ACS Photonics* **2018**, *5*, 3936.